Femtosecond lasers in fluid inclusion analysis:

Overcoming metastable phase states

Running title: Overcoming metastable phase states using femtosecond lasers

Outline:

Corresponding author:
Yves Krüger, lfa@fluidinclusion.ch,
LFA – Labor für Fluideinschluss-Analytik
Cäcilienrain 3
CH-3007 Bern, Switzerland
Tel. +41 31 371 31 52

Number of characters (including spaces): 60,160 (Microsoft Word 2003 on Windows XP)

Femtosecond lasers in fluid inclusion analysis:

Overcoming metastable phase states

Yves Krüger[1]*, Patrick Stoller[2], Jaro Rička[2], Martin Frenz[2]

[1]LFA – Labor für Fluideinschluss-Analytik, Cäcilienrain 3, CH-3007 Bern

[2]Institut für angewandte Physik, Universität Bern, Sidlerstrasse 5, CH-3012 Bern

Abstract

We have developed a new method to overcome metastable phase states that prevent microthermometric measurements in fluid inclusions. We use tightly focused femtosecond laser pulses to induce bubble nucleation in one-phase (all liquid) inclusions, nucleation of salt crystals in supersaturated brines, and nucleation of ice and salt hydrates. The threshold laser intensity necessary for phase nucleation was determined to be of the order of 10 TW/cm^2. To avoid potential damage to the fluid inclusion, the threshold for producing ablation of quartz visible under the microscope was also determined and found to be about 25 % higher than the threshold for halite nucleation and 100 % higher than that for bubble nucleation. The experimental setup allows us to induce phase nucleation in selected fluid inclusions at different temperatures under microscopic observation. Subsequent microthermometric measurements can be performed in the same setup, making it suitable for routine applications.

Keywords: femtosecond laser, fluid inclusions, metastable phase state, nucleation, threshold, microthermometry

* Corresponding author:
e-mail lfa@fluidinclusion.ch
www.fluidinclusion.ch

1. Introduction

Metastable fluid states, particularly the absence of a thermodynamically stable phase under specific P-V-T-X conditions, are characteristic features of microthermometric measurements of fluid inclusions, and they can be extremely helpful for precise temperature determination of phase transitions if these cannot be observed directly. The temperature cycling method, as described for example in Goldstein & Reynolds (1994), makes use of the temperature gap between the disappearance and the nucleation of phases due to metastable states. It can be applied to the determination of the final melting temperatures of ice and solid CO_2, the dissociation temperatures of gas clathrates and salt hydrates, the dissolution temperatures of salt crystals, and, in the case of homogenization to the liquid phase, the homogenization temperatures of CO_2 and total fluid.

On the other hand, the metastable temperature delay on phase nucleation can also cause analytical problems when nucleation of, for example, the vapour bubble, ice or salt hydrates or salt crystals in supersaturated brines fails to occur, and thus prevent microthermometric determination of the corresponding phase transitions such as hydrate dissociation, ice melting, salt dissolution, and homogenisation of the fluid (ref. Roedder, 1984; Goldstein & Reynolds, 1994; Arnold, 1986; Weisbrod & Leroy, 1987; Roedder & Belkin, 1988). For example, in minerals formed under supergene to low-temperature (hydrothermal) conditions metastable one-phase inclusions are common. Current methods used to circumvent metastable phase states by stimulating phase nucleation are described, for example, in Sterner et al. (1988) and Goldstein & Reynolds (1994), but, in many cases, are not effective.

The present study addresses this problem and presents a new method to reliably and repeatedly overcome metastable fluid states using femtosecond laser pulses, thus enabling microthermometric

measurements. In Section 2 of this paper, we summarize the conditions under which phase nucleation is often observed to fail and discuss the limits of current methods used to overcome metastability. We do not provide an exhaustive list of such conditions but seek instead to demonstrate the broad applicability of the new technique. In Section 3 we describe the experimental setup used to overcome metastable phase states in different inclusions and under different temperature conditions; the results of these experiments are presented in Section 4. The laser intensity must be carefully controlled to prevent damage to the fluid inclusions. We report laser intensity thresholds necessary to achieve nucleation and to visibly ablate the quartz in Section 5. Here we also note the limitations of the different microscope objectives used to focus the laser beam; these determine the minimum pulse energy required to induce phase nucleation at a given depth in the sample. In Section 6.1 we discuss possible mechanisms for the nucleation of different phases using tightly focused femtosecond laser pulses in the context of recent studies of ultra-short pulse laser ablation (Stuart et al., 1996; Vogel et al., 2005; Joglekar et al., 2004). Finally, we discuss the possibility of laser induced volume changes to the inclusion and note how these can be minimized or avoided completely (Section 6.2).

2. Metastable phase states

2.1 Metastable one-phase (liquid) inclusions

In many fluid inclusions formed at diagenetic or low grade metamorphic conditions one observes metastable one-phase inclusions at room temperature containing only the liquid phase of the aqueous solution. In H_2O-salt inclusions the vapour bubble buffers the fluid pressure, and its metastable absence prevents use of the hydrate dissociation and ice melting temperatures in the

determination of salt composition and salinity. Absent a vapour bubble, the fluid pressure is unknown and not defined by equilibrium conditions. Therefore, microthermometric measurements of these phase transitions always require the presence of the vapour bubble (see 2.2). Additionally, the metastable absence of the vapour bubble obviously prevents determination of the homogenization temperature T_h by heating the sample and thus estimation of the trapping conditions of the inclusions.

A current method to stimulate bubble nucleation for subsequent T_h measurements is storing the inclusions at – 10 °C (well above ice nucleation) for several days or weeks (Newell & Goldstein, 1999). This trick sometimes works, but in many cases it does not. Therefore, we sought to find a reliable and fast method by which it is possible selectively to induce bubble nucleation at room temperature without resulting in any volume change of the inclusion. This would then allow measurement of T_h.

Roedder (1984) presents a theoretical, qualitative picture of bubble nucleation: On cooling of an inclusion with homogeneous liquid, differential shrinkage of the liquid and the surrounding host mineral leads to stretching of the liquid and may result in negative pressures (tension) within the inclusion. If tension forces in the liquid become high enough, a vapour bubble nucleates and the fluid pressure increases instantaneously to equilibrium conditions. Zheng et al. (1991) investigated experimentally the P-T-field of the thermodynamic metastability of liquid water using synthetic fluid inclusions. In this field, bounded by the liquid-vapour-curve and the spinodal, the liquid state of the water is mechanically stable. The spinodal, which originates at the critical point of water, extends to negative pressures (tension in the liquid) and reaches a minimum of approximately – 1400 bar at 42 °C. According to the interpretation of Zheng et al. (1991), which is based on the stability limit conjecture proposed by Speedy (1982) the spinodal returns to positive pressure at

lower temperatures. This re-entrant spinodal, however, is the subject of current debate (Poole et al., 1992; Sastry et al., 1996; Debenedetti, 2003; Speedy 2004; Debenedetti 2004).

We have found empirically that for aqueous, low saline, and practically gas free inclusions in quartz with sizes between 2 and 10 µm, failure of bubble nucleation often occurs at fluid densities that correspond to homogenization temperatures below about 120 to 140 °C. In two phase inclusions displaying T_h values between 120 and 140 °C, the vapour bubble nucleates approximately 50 to 70 °C below T_h on cooling. It is thus likely that metastable one-phase inclusions, where nucleation of the vapour bubble failed, have T_h-values below 140 °C. In many studies, T_h-values well below 100 °C have been reported (e.g. Boiron et al., 2002; Jonsson & Broman, 2002), which is explained by the fact that several factors may influence whether and how far below the homogenization temperature bubble nucleation occurs. We distinguish between factors that are likely to affect homogeneous nucleation—where the mechanical instability of the metastable state alone suffices—and those likely to affect heterogeneous nucleation—where a nucleation site leads to a local reduction of the activation energy of the phase transition. Factors influencing homogeneous nucleation include the salinity of the solution and the gas content of the fluid, which can both influence the cohesion forces of the liquid, as well as the host mineral itself (Zheng et al., 1991). The presence or absence of tiny solids within the inclusions and the structure of the inclusion walls can both influence heterogeneous nucleation. It has also been observed in many studies (Roedder, 1984) that failure of bubble nucleation is more likely to occur in the smallest inclusions; larger inclusions formed under the same conditions often have two phases present at room temperature. Roedder (1984) explained this using a surface-tension model, according to which a bubble of less than approximately 1 µm in diameter cannot be stable and would have to collapse instantly after nucleation. He also states that "the smallest stable bubbles found in any inclusions are those in small low-temperature, highly saline inclusions close to

homogenization temperature. These bubbles can be well under 1 micrometer in diameter." In this study, however, we found that the effect of surface-tension must be smaller than Roedder (1984) assumed and that vapour bubbles with diameters well below 1 μm are still stable in pure water and low saline inclusions. An alternative explanation for the absence of bubbles from smaller inclusions is that, since the number of heterogeneous nucleation sites in a fluid inclusion likely depends on its size, smaller inclusions are simply more likely not to have a nucleation site at all.

2.2 Metastable ice melting

For determination of the correct ice melting temperature ($T_m ice$)—which is used to determine the salinity of the aqueous solution—the fluid inclusions must contain a vapour bubble (L+V+ice → L+V), otherwise the phase transition proceeds under metastable phase conditions and may result in positive $T_m ice$-values. Apart from those fluid inclusions which are already metastable one-phase at room temperature (see 2.1), there are also low saline (below 5 - 7 wt% salt) inclusions that are two-phase at room temperature, but do not contain a vapour bubble during the ice melting process. The homogenization temperature of these two-phase inclusions is typically below about 150 °C.

On freezing and nucleation of the ice, the vapour bubble in the (low saline) two-phase inclusions is completely compressed due to volume expansion of the ice. After ice nucleation, the inclusion contains ice and a small amount of metastable salt-rich liquid (L_1+V → L_2+ice), as the spontaneous nucleation of salt hydrates usually occurs at lower temperatures than the ice nucleation temperature. During subsequent heating the ice melts continuously, but in the absence of the vapour bubble $T_m ice$ is shifted to higher values and it can often be observed that ice melts instantaneously at the moment of bubble nucleation, sometimes even at positive temperatures. This shift of the ice

melting temperatures can be explained by negative pressure in the inclusion due to the metastable absence of the vapour bubble (Roedder, 1984); when the vapour bubble forms, pressure increases to equilibrium conditions (liquid-vapour curve) and ice is no longer stable.

Since the ice melting temperatures in H_2O-salt inclusions do not depend on the fluid density (i.e. are independent of the bubble size) current methods circumvent the problem of metastable liquid inclusions by stretching the inclusions (irreversible volume expansion) to form a vapour bubble, as described in Goldstein & Reynolds (1994). In weak host minerals like calcite, stretching of the inclusions may already occur due to the volume expansion of the fluid resulting from ice nucleation. The other method, described by the same authors, to expand the inclusion volume is to heat the inclusions well above T_h and leave them for several hours at high internal fluid pressures. The reliability of this procedure is poor and it often results in total decrepitation of the inclusions. Both of these techniques for stretching fluid inclusions have the additional disadvantage that they are not selective: chance determines which inclusions will form a vapour bubble and which will not. With our new method we can induce bubble nucleation in selected fluid inclusions at temperatures below the true ice melting temperature by incorporating a heating/freezing stage in the experimental setup. Stretching of an inclusion is not a prerequisite for bubble nucleation using our technique, and, in most cases where the inclusion volume did not expand as a result of ice nucleation, bubble nucleation also did not result in volume expansion.

2.3 Metastabilities of supersaturated salt solutions

Slightly supersaturated salt solutions in fluid inclusions tend to be metastable at room temperature and do not contain daughter crystals such as halite (NaCl) or sylvite (KCl). In many

cases precipitation of the salt crystals can be achieved by freezing the inclusions and subsequently slowly heating them (Sterner et al., 1988), but in some cases this method does not work. In supersaturated brines, salinity cannot be determined from the melting temperature of ice, but can only be determined from the dissolution temperature of the salt crystals or, depending on salt composition and concentration, from the dissociation of a salt hydrate, for instance of calcium chloride ($CaCl_2$).

Apart from the failure of salt-precipitation, it has also been observed that the supersaturated liquid remains stable even after supercooling to – 190 °C, i.e. no ice or hydrate phase nucleates (Roedder, 1984). Subsequent slow heating may result in nucleation of ice or salt hydrates but this is not guaranteed and the procedure is time consuming. We therefore used femtosecond laser pulses to induce precipitation of salt crystals at room temperature and nucleation of ice and hydrohalite at – 56 °C.

3. Experimental setup

We used an amplified femtosecond (1 fs = 10^{-15} s) laser system in these experiments and tightly focused the laser beam using high numerical aperture microscope objectives. Femtosecond lasers, which have pulse durations on the order of a few hundred femtoseconds or less, deliver very high peak powers without depositing very much energy into a sample; thermal effects are avoided. For instance, a 100 fs laser pulse with the same peak power as a 100 ns laser pulse contains 10^6 times less energy. The highly nonlinear process through which laser energy is coupled to the sample leads to well-defined intensity (sometimes alternatively referred to as irradiance) thresholds for different physical effects, such as visible sample ablation (Vogel et al., 2005). By focusing the laser beam

using a high numerical aperture microscope objective, the region in which this threshold is exceeded can be tightly confined to a volume of less than 1 μm^3.

The experimental setup schematically shown in figure 1 consists of a Coherent Mira femtosecond Ti:sapphire oscillator (wavelength 800 nm) and a Coherent RegA amplifier with a nominal maximum output pulse energy of 4 μJ and a full-width at half-maximum pulse duration of around 330 fs (the pulse width was measured using a Carpe auto-correlator). The Mira laser is pumped with a Coherent Verdi 6 W Nd:YVO_4 diode-pumped solid state laser in order to achieve a population inversion. The RegA is seeded using the Mira and pumped with a Coherent Verdi 10 W Nd:YVO_4 diode-pumped solid state laser: pulses from the Mira are selected and then amplified approximately 1000-fold by the RegA. A detailed discussion of the construction and operation of femtosecond lasers is found in (Koechner, 1999). The RegA can be operated in a single-pulse mode where laser pulses are triggered at the push of a button. When the RegA is not pulsing, a small fraction of the Mira seed beam leaks through and can be used for aligning the laser onto a specific fluid inclusion without affecting the sample. The laser beam from the RegA is directed via protected silver mirrors through a $\lambda/2$-plate (HWP) and then through a Glan-laser polarizer. The rotatable HWP is used to adjust the energy of the laser pulses. The beam then passes through a spatial filter and a 2x beam expander consisting of a 100 mm focusing lens, a 75 μm pinhole and a 200 mm collimating lens. A maximum pulse energy of around 0.8 μJ was measured after the 200 mm collimating lens. The beam is coupled into an Olympus BX51 upright microscope through the additional port provided by an Olympus UD-P dual port adapter with an XF 2033 dichroic mirror for multiphoton microscopy (Omega Optical). The microscope used is equipped with an Olympus LMPlanFL 100x/0.80 long working distance objective (no coverglass correction), an Olympus UPlan FL N 60x/0.90 objective (with a correction ring for coverglass thickness from 0.11 to 0.23 mm), and an Olympus PLAPO 100x/1.40 oil immersion objective. Since the size of the back-

aperture of the different objectives is not the same, the lenses in the beam telescope were chosen to expand the beam to optimally fill the back-aperture of the 60x/0.90 and the 100x/1.40 oil-immersion objective. This results in overfilling of the 100x/0.80 dry objective. This does not significantly affect the quality of the focus, but does reduce the laser power that is coupled through that objective. In conjunction with the 60x objective we used a U-CA Magnification changer (magnification factor 1.6x). A high sensitivity monochrome digital camera (pco.1600) was mounted on the microscope's camera port to observe both the fluid inclusions in transmitted light and the back-scattered 800 nm light from the laser spot (transmission of the dichroic mirror is about 1 %). Filters to completely block the laser light (3 mm thick Schott BG39 glass) were placed inside the eyepieces to ensure that eye damage could not occur if the user accidentally looked through the eyepieces during pulsing of the laser. A Linkam THMSG 600 heating/freezing stage was mounted on the microscope in order to perform low temperature experiments and microthermometric measurements. Temperature was controlled by a Linkam TMS 94 temperature controller and the stage was cooled using a liquid nitrogen pump (LNP/2) from the same company.

The experimental setup and the use of dry objective lenses allows us to induce phase nucleation in selected fluid inclusions at different temperatures under microscopic observation and to perform subsequent microthermometric measurements without moving the sample. Amplified Ti:sapphire lasers are available as single, software-controlled units and the 800 nm wavelength at which they operate most efficiently can be focused using conventional microscope objectives and coupled into the microscope using commercially available optics designed for multiphoton microscopy. This system is therefore suitable for routine applications.

4. Results

For our investigations we used natural and synthetic fluid inclusion samples prepared as sections of approximately 250 μm thickness and polished on both sides. The samples were loaded into the heating/freezing stage and brought to the appropriate temperature. Inclusions were selected in transmitted light, and the laser spot was focused onto the inclusions. Only a single laser pulse of appropriate intensity was necessary to induce phase nucleation. Because high pulse energies can result in damage to the inclusions, we determined the appropriate pulse energy by measuring the threshold of visible quartz ablation far from the inclusion but at the same depth in the bulk material; we found that the threshold energy for phase nucleation can be estimated from the threshold for visible quartz ablation. The ablation thresholds for visible quartz ablation and phase nucleation using the different microscope objectives are discussed in detail in Section 5 below. The images in figures 2.1-4.3 show examples of phase nucleation in fluid inclusions using single femtosecond laser pulses and are discussed in detail below.

4.1 Nucleation of the vapour bubble at room temperature

In order to determine T_h in metastable one-phase inclusions we induced bubble nucleation by means of single femtosecond laser pulses. Any irreversible volume expansion of the inclusions caused by the laser pulses, however, would increase T_h values and could make the method unsuitable for this purpose. We therefore tested our method by repeated bubble nucleation and measurements of T_h in the same inclusions. We performed the experiments using natural, secondary, one-phase inclusions in quartz, a mineral which is known to resist high fluid pressures in the inclusions (Roedder, 1984) and primary, one-phase inclusions in calcite, a mineral which cannot withstand high pressures due to its relatively low hardness and cleavage along {1011}. As

metastable one-phase inclusions often occur as small inclusions, we applied our method to inclusion sizes down to 1 µm.

Figure 2.1 shows an example of laser induced bubble nucleation in a 5 µm one-phase inclusion in quartz before (a) and after (b), (c) the laser pulse . Note the second vapour bubble in image (b) which disappeared within $^{1}/_{30}$ sec (the frame rate of the camera was 30 frames/sec). Repeated measurements of T_h all yielded 76.8 °C and confirmed that no volume expansion of the inclusion occurred as a result of the femtosecond laser pulse. We also induced bubble nucleation in a 2 µm inclusion in quartz (not shown). The size of the vapour bubble was at the limit of the optical resolution and only the rapid movement of the bubble allowed identification and observation during microthermometry. T_h was determined repeatedly to be 74.0 °C, excluding the possibility of any volume change of the inclusion.

Figure 2.2 shows an example of bubble nucleation in a 10 µm one-phase inclusion in calcite before (a), (b) and after (c), (d) the laser pulse. The position of the laser spot can be seen in the images (b) and (c). Repeated measurements of the homogenization temperature confirmed that inclusions in calcite also do not change volume, and the T_h determined was 63.8 °C. We also achieved bubble nucleation in a 1.5 µm one-phase inclusion in calcite (not shown). The vapour bubble could hardly be recognized in single image frames but its fast movement allowed identification in live observation during microthermometry. T_h was determined to be 59.7 °C in repeated measurements.

4.2 Nucleation of the vapour bubble below the ice melting temperature

For these experiments we only used fluid inclusions in quartz because calcite does not withstand the internal pressures on the inclusion walls arising from the volume expansion of the ice. The irreversible volume expansion of inclusions in calcite and some other minerals due to ice nucleation can be sufficiently high as to result in spontaneous bubble nucleation upon subsequent heating, allowing determination of $T_m ice$ (refer to Section 2.2). Quartz, however, can usually withstand the pressure arising from ice nucleation and therefore bubble nucleation has to be induced by single laser pulses. Since inducing bubble nucleation only 0.2 °C below $T_m ice$ did not heat the inclusion enough to result in complete melting of the ice, we can conclude that the laser pulse does not significantly heat the fluid inclusions. This is in good agreement with the observations and the calculations of Vogel et. al. (2005), who determined that the total energy deposited in the plasma during femtosecond water ablation near the threshold using comparable laser parameters was less than 20 pJ (the energy deposited during ablation of quartz should be of a similar order of magnitude; 1 pJ = 1 picojoule = 10^{-12} J).

Figure 3.1 shows bubble nucleation in a natural one-phase inclusion at – 14.0 °C in the presence of ice (L+ice → L+V+ice) before (a) and after (b)-(d) the laser pulse. The final ice melting temperature ($T_m ice$) was determined to be – 9.9 °C, corresponding to approximately 13.9 wt% NaCl equivalent in the solution (Potter et al., 1978). Due to the high salinity of the fluid, the amount of liquid at – 14.0 °C is relatively large compared to the amount of ice.

Figure 3.2 shows an example of bubble nucleation in a low saline natural one-phase inclusion at – 1.4 °C in the presence of ice (L+ice → L+V+ice) before (a) and after (b)-(d) the laser pulse. $T_m ice$ was determined to be – 0.9 °C, corresponding to approximately 1.6 wt% NaCl equivalent in the solution (Potter et al., 1978). The amount of liquid at – 1.4 °C is small compared to the amount of ice, resulting in a strongly compressed bubble. Subsequent measurement of T_h showed a relatively

large increase from 76.8 to 110.7 °C, indicating an increase in the inclusion volume. A T_h of 110.7 °C was then measured after several additional nucleation cycles, which means that inclusion volume did not increase any further. In gas-free aqueous inclusions, volume changes have no effect on $T_m ice$. However, inclusions containing some low density gas will show slightly higher $T_m ice$ values due to the negative slope of the ice-melting-curve in P-T-space because gas pressure decreases when inclusion volume increases.

4.3 Nucleation of solids

For these experiments we used two synthetic fluid inclusions samples, one containing a 29.1 wt% KCl solution and the other containing a 29.9 wt% NaCl solution. Both were supersaturated at room temperature. The fluid inclusions were synthesized following the principles described by Bodnar & Sterner (1987). The inclusions containing the KCl solution were metastable with respect to sylvite but with liquid and a vapour bubble present at room temperature. In contrast, the inclusions containing the NaCl solution were metastable with respect to both halite and the vapour bubble, having only the liquid phase present at room temperature.

Figure 4.1 shows the nucleation and subsequent crystallization of sylvite from the supersaturated KCl solution at room temperature. Prior to inducing sylvite nucleation we determined T_h to be 182.5 °C. Image (a) shows the inclusion and the position of the laser spot before the laser pulse. After initial nucleation induced by the laser pulse (at the position of the laser spot), sylvite precipitated from the supersaturated solution and re-crystallized continuously as shown in the images (b)-(e). The sylvite dissolution temperature was determined to be 42.2 °C and T_h increased slightly to 188.5 °C, reflecting a slight increase of the inclusion volume. According to

the polynomial fit determined by Sterner et al. (1988), a 29.1 wt% KCl solution corresponds to a sylvite dissolution temperature of 42.8 °C.

Figure 4.2 shows the nucleation and subsequent crystallization of halite after the vapour bubble was previously induced. T_h was determined to be 121.4 °C. Image (a) shows an inclusion containing two phases (L+V) before and images (b)-(d) after the laser pulse that induced halite nucleation. The formation of small vapour bubbles can be observed in image (b); one formed right beside the large bubble and the other one close to the position of the laser spot. Both of the secondary vapour bubbles disappeared immediately. The halite crystal nucleated at the position of the laser spot and grew quickly. The halite dissolution temperature was measured to be 136.8 °C and T_h increased to 132 °C after several halite nucleation cycles. Using the results of Sterner et al. (1988) and assuming that halite dissolution proceeds in the presence of liquid and vapour, the measured dissolution temperature corresponds to 29.2 wt% NaCl, whereas the initially loaded salinity of the solution for synthesis of the inclusions was determined to be 29.9 wt% and would yield a dissolution temperature of 156.1 °C. Considering the strong dependence of halite dissolution temperatures on salinity, the measured 136.8 °C are in good agreement with the prediction derived from the polynomial fit of Sterner et al. (1988). The small difference in salinity of 0.7 wt% NaCl can be attributed to experimental uncertainty related to the synthesis of the fluid inclusions and possibly to uncertainty in the polynomial fit; it cannot be explained by the fact that halite dissolution was observed in the absence of the vapour phase at a temperature slightly above liquid-vapour homogenisation, since this effect, which is small, results in a shift to higher temperatures. Volume changes of the inclusion may influence salt dissolution temperatures (see Sterner et al., 1988), but the resulting error in the determination of the total salinity is small and could, if necessary, be corrected using the initially measured T_h value.

The same inclusion as shown in figure 4.2 was also used for another experiment: The inclusion, which initially contained two phases (L+V) at room temperature, was cooled down to – 120 °C and subsequently slowly heated. This procedure, already mentioned in section 2.3 did not result in spontaneous nucleation of ice and/or hydrohalite. We therefore used a single laser pulse to induce phase nucleation; this is shown in figure 4.3. The inclusion was cooled to – 56 °C (a) and then the laser pulse induced nucleation and fast crystallization of ice, best visible in images (b) and (c), and hydrohalite (HH, $NaCl \cdot 2H_2O$), best visible in images (d) and (e). The vapour bubble is thereby strongly compressed (L_1+V → ice+HH+V). We found that ice and hydrohalite nucleation could not be achieved at temperatures higher than – 56 °C. In that case, only formation of secondary vapour bubbles was induced by the laser pulse, or, if the pulse intensity was set high enough, halite nucleated. On subsequent heating, ice re-crystallized and then melted at the eutectic temperature of the H_2O-NaCl system (– 21.2 °C) illustrated in images (g)-(j) (ice+HH+V → L_2+HH+V). On further heating hydrohalite dissociated continuously, as shown in images (k) and (l) and the final dissociation temperature of hydrohalite was measured to be 20.2 °C (L+V+HH → L_1+V). In a stable phase assemblage hydrohalite should dissociate at + 0.1°C under simultaneous formation of halite. Because halite did not nucleate, hydrohalite remained metastable up to 20.2 °C.

5. Threshold intensities for quartz ablation and phase nucleation

In order to avoid damaging the fluid inclusions, which can result in an irreversible volume expansion, it is important to use pulse energies close to the threshold for phase nucleation. The threshold pulse energy necessary to induce phase nucleation is strongly dependent on the quality of the laser beam focused by the microscope objective. Therefore, we used a spatial beam filter to ensure a good initial beam quality. Furthermore, a beam-profiling camera was used to confirm that

a nearly Gaussian spatial profile was achieved. The properties of the microscope objectives used also have a major influence on the threshold pulse energy. The numerical aperture (N.A.) of the objective and the spherical aberration of the objective-sample system (as well as other optical aberrations) must be taken into account. For a given wavelength, the numerical aperture defines the smallest achievable spot size of the focused laser beam, which is proportional to $1/N.A.^2$. Therefore, for the same pulse energy, a higher numerical aperture results in a higher peak laser intensity. For this reason, oil immersion objectives with N.A. up to 1.40 would be the best choice to obtain tight focusing, but these are not practical for our purpose since the immersion oil cannot be exposed to temperature extremes. The 0.8 and 0.9 N.A. dry objectives used are suitable for microthermometry in small fluid inclusions at low temperatures; the long working distance 0.8 N.A. objective was also used when heating the sample to homogenization temperatures. A disadvantage of microscope objectives with a numerical aperture of less than 0.9 is that self-focusing of the laser beam may occur at the laser powers necessary for femtosecond laser ablation (Vogel et al., 2005). Briefly, self-focusing occurs because materials can have an intensity dependent index of refraction which leads to a higher index of refraction at the centre of a beam than at the edge (for a detailed discussion, refer to Boyd, 2003). Because self-focusing depends only on the laser power and not the intensity, this effect is not seen at higher numerical apertures, where lower laser powers suffice to achieve the intensities necessary for ablation.

Assuming that the microscope objective's back-aperture is optimally filled or somewhat overfilled, that spherical aberration can be neglected, that nonlinear self-focusing of the beam does not occur, and that the incident beam has a Gaussian spatial profile, we can assume a diffraction-limited spot-size (refer, for instance, to Novotny & Hecht, 2006). The diffraction-limited focal spot diameter is approximately 640 nm, 570 nm, and 360 nm at the 1/e intensity for the 0.8 N.A., 0.9 N.A., and 1.4 N.A. objectives, respectively. This allows us to calculate a *nominal* intensity at the

focus from a measurement of the pulse duration and of the pulse energy after the microscope objective. The *actual* intensity at the focus will depend on how well the conditions given above are met. While proper filling of the objective and a Gaussian spatial profile of the beam can readily be achieved, spherical aberration often leads to a significant increase in the focal spot size if the focused beam propagates through a boundary where the optical index of refraction changes (Török et al, 1995). The boundaries between air and quartz and between immersion oil and quartz (in the case of an oil-immersion objective) represent a large and a relatively small change in the index of refraction, respectively. Furthermore, a microscope objective with a fixed cover-slip correction will only work optimally at one depth in the sample; the fact that quartz ($n_o = 1.544$, $n_e = 1.553$) has a different index of refraction from that of a cover glass ($n = 1.516$) means that this correction will never be perfect. The performance of oil-immersion objectives or dry objectives with a cover-slip thickness correction ring will also be limited by this small difference in the index of refraction due to spherical aberration. High numerical aperture objectives are likely to be more sensitive to this index difference.

To determine the effect of these limitations on microscope objective performance on our femtosecond laser nucleation technique, we determined the pulse energy necessary to achieve the threshold for visible quartz ablation as a function of depth within a quartz sample for several different microscope objectives. In Figure 5, we plot the threshold pulse energy as a function of the depth of the laser focus in the sample; the threshold pulse energy is normalized to the minimum pulse energy required for visible ablation for each objective. Using the 60x/0.90 objective with its correction ring set to 0.11 mm, the *nominal* pulse energy threshold for visible quartz ablation reaches a minimum approximately 0.08 mm below the surface. For a correction ring setting of 0.17 mm the minimum is at around 0.11 mm but the change in pulse energy threshold with depth is more pronounced than for the 0.11 mm correction. For the 100x/0.80 objective, which is built for use

without a cover-glass (0 mm cover-glass correction), the pulse energy threshold increases continually with depth, as expected. We also measured pulse energy thresholds with the Olympus PLAPO 100X/1.40 oil immersion objective. We found that the minimum threshold again lies at the surface of the sample and increases with depth, though not as rapidly as for the dry objective. The pulse energy profiles in figure 5 clearly show that the threshold energy for quartz ablation is dependent on the depth within the sample. Thus, a completely satisfying correction of the spherical aberration in the quartz samples can neither be achieved using a correction ring for cover glass thickness nor using oil immersion.

For the 100x/0.80 and the 100x/1,40 oil objective lenses, which both have minimum pulse energy threshold at the sample surface, we calculated *nominal* laser threshold intensities at the focus (using the paraxial approximation) of approximately 24 and 25 TW/cm^2 (1 TW = 1 TeraWatt = 10^{12} W) for visible quartz ablation at the surface. This indicates that self-focusing likely does not occur, even when the 0.8 N.A. objective is used. The value for the minimum *nominal* threshold with the 60x/0.90 objective is calculated to be approximately 46 TW/cm^2. The threshold intensity for ablation is a property of the material. The fact that the *nominal* intensity at the quartz ablation threshold is almost twice as high for the 60x objective likely results from a spot size larger than the diffraction limit caused by spherical aberration.

The depth dependence of the threshold pulse energies that we observed for quartz ablation is, of course, also valid for phase nucleation in the fluid inclusions. We found that for bubble nucleation at room temperature only 50-60 % and for halite nucleation 70-80 % of the energy required for visible quartz ablation is necessary. Figure 6.1 illustrates laser induced bubble nucleation in a supersaturated H_2O-NaCl one-phase inclusion at room temperature. The pulse energy was about 50 % of the energy used for visible quartz ablation in the bulk material at the same depth within the

sample. Simultaneous nucleation of the vapour bubble and halite in the same inclusion is shown in figure 6.2. The pulse energy was approximately 70 % of the energy used for visible quartz ablation. These results were at first sight rather surprising, and have had a major influence on our understanding of the process that leads to phase nucleation when fluid inclusions are irradiated with femtosecond laser pulses.

6. Discussion

6.1 Possible mechanisms of phase nucleation

At the beginning of this study, we hypothesized that focusing the femtosecond laser into an inclusion would lead to generation of a plasma and formation of a cavitation bubble in the liquid as described by Vogel et al. (2005). Our initial hypothesis was contradicted by the experimental evidence gathered in this and in a previous study: According to Schaffer et al. (1998) the threshold for formation of a cavitation bubble in water using femtosecond laser pulses by multiphoton ionization is approximately 2.5 times higher than the threshold for quartz ablation. Thus, phase nucleation within the metastable fluid, which we have observed to have a threshold below that of visible quartz ablation, is unlikely to result from a laser induced cavitation bubble in the liquid. However, in fluid inclusions that already contained a vapour bubble, on application of a laser pulse, we observed movement of the vapour bubble and formation of small secondary bubbles which rapidly disappeared (see Fig. 4.2). This suggests that the laser pulse induces a pressure wave in the inclusion that also produces tensile forces, which result in the formation of secondary vapour bubbles. Although pulse intensities are below the visible threshold for quartz ablation, we suggest that the pressure wave is produced by sub-microscopic quartz ablation at the inclusion walls. This is

supported by the following observations:

1. Phase nucleation due to pulses at the threshold intensity depends strongly on the z-position of the laser focus in the inclusion, and, at intensities well above phase nucleation threshold, visible quartz ablation occurs near the top surface of the inclusions. However, it is not easy to determine the exact z-position of the laser focus because it does not coincide exactly with the focus of the visible light. This is due to chromatic aberration, which is not corrected up to 800 nm in the microscope objective. From our quartz ablation experiments we assume that the offset of the laser focus can be up to 2 – 3 μm, which is fairly large considering the scale of fluid inclusions. In future investigations we will try to determine the z-position of the laser focus exactly using second harmonic generation microscopy to image the inclusion walls (Stoller et al. 2007).

2. We performed experiments in which the laser was focused a few μm beside the fluid inclusion and pulse intensities above the threshold for visible quartz ablation were used. We found that the pressure wave emitted induced phase nucleation in the inclusions. Figure 7 shows nucleation of the vapour bubble with a pulse intensity approximately 6 % above the ablation threshold and halite nucleation with a pulse intensity approximately 30 % above the ablation threshold.

Based on these two observations we suggest that phase nucleation in the metastable fluid inclusions is induced by the pressure wave emitted from sub-microscopic quartz ablation at the surface of the fluid inclusion by single femtosecond laser pulses. Because the plasma that forms during ablation forms within several picoseconds—a much shorter time than the mechanical stress wave takes to traverse the focal region—a compression-rarefaction wave is expected to form during femtosecond laser ablation (Vogel et. al. 2005); ablation leading to a stress wave may occur without

producing damage visible under an optical microscope (Joglekar et al., 2004). We note that nanoscopic debris from ablation of quartz at the inclusion surface could by itself lead to heterogeneous nucleation of phases in the sample.

6.2 Volume changes of the inclusions

Volume changes of the inclusions in connection with femtosecond laser pulses and phase nucleation have already been mentioned in section 4. Changes of the inclusion volume can be observed indirectly by measuring homogenisation temperatures. We found clear evidence that re-opening of micro-capillaries that once connected single cavities during the healing process of fractures seems to be the major mechanism for volume expansion and can explain increases in homogenisation temperatures of more than 30 °C; these micro-capillaries are sometimes visible under the microscope. Especially large volume changes occur when two previously separated inclusions are joined again by a micro-capillary. We assume that such healed structures represent weak spots in the crystal lattice which can be cracked most easily by the pressure wave resulting from the laser pulse. We therefore can deduce that volume expansion occurs most likely in secondary and pseudo-secondary inclusions, but not in primary ones. A common feature resulting from the pressure wave is a disturbance of and sometimes even disruption of the vapour bubble in L-V-inclusions. This is strongly dependent on the initial pulse energy and the z-position of the laser focus.

On the other hand, we did not find evidence that visible ablation of quartz from the inclusion walls, observed many times during our experiments when pulse intensities well above the nucleation threshold were used, results in measurably increased T_h values. The ablated quartz

volumes are probably too small compared to most inclusions volumes and therefore quartz ablation is likely only relevant in the very smallest inclusions.

As already noted before, volume expansion of the fluid inclusions are most critical for determination of the homogenisation temperatures. In our experiments, increases in the homogenisation temperature after bubble nucleation at room temperature were rarely seen and were usually less than 0.5 °C. One reason for this might be that bubble nucleation requires the lowest pulse intensities of all of the nucleation processes. In all other cases where volume expansion occurs, it does not have an effect on the determination of the phase transition temperatures, as discussed above. Furthermore, by using laser pulse intensities close to threshold the likelihood of volume expansion of the inclusions can be strongly reduced.

6. Conclusions

In this study we have presented a reliable and highly efficient method to overcome metastable fluid states that prevent microthermometric measurements or could until now only be overcome by applying time consuming temperature cycling procedures. The method allows us to induce phase nucleation in fluid inclusions down to 1 μm in size and in different host minerals. We have thus shown that the minimum mechanically stable bubble size of approximately 1 μm in pure water predicted by Roedder (1984) is not accurate and bubbles well below this size are stable. Volume expansion of the inclusions may occur but can be prevented or minimized by using pulse intensities near the nucleation threshold. The experimental setup we have used is suitable for routine applications.

An additional application of the new method, which could not be tested in the course of this study, concerns the nucleation of salt hydrates. Nucleation of the salt hydrates usually requires a time consuming temperature cycling procedure and fails in many cases (Bakker, 2004).
Based on our experience with supersaturated NaCl solutions, however, it is likely that femtosecond laser pulses can also be used to induce nucleation of salt hydrates like hydrohalite ($NaCl \cdot 2H_2O$) or antarcticite ($CaCl_2 \cdot 6H_2O$) in under-saturated solutions, presumably at temperatures between – 60 and – 90 °C. However, the experimental setup would require coupling the femtosecond laser into the microscope light path of a micro-Raman-spectrometer, in order to subsequently detect and identify the hydrate phases. Using Raman-spectroscopy it is possible to identify relatively small amounts of different salt hydrates in fluid inclusions (Samson & Walker, 2000).

The novel technique presented in this paper opens a vast new field of applications of fluid inclusion research that reaches beyond the realm of geology. For example, laser induced bubble nucleation can be used to determine formation temperatures of speleothems, which was not possible to date and which is of great importance for paleoclimate research. In addition, this method allows determination of temperature conditions of mineral formation in supergene ore deposits directly from fluid inclusion microthermometry data. Finally, the method also provides new possibilities to investigate the properties of metastable water in a pressure and temperature regime near the homogeneous nucleation limit of super-stretched and super-cooled water that is difficult to access experimentally.

Acknowledgements. We thank Monika Painsi and Dr. Nicklaus Waber from the Institute of Geological Sciences at the University of Bern for providing fluid inclusion samples, and we are grateful to Jörg Baumgartner of Olympus (Switzerland) AG for generously loaning us the PLAPO 100X/1.40 oil immersion objective lens. We thank Dr. Dubessy, Dr. Ramboz, Dr. Van den Kerkhof.

and an anonymous reviewer for their constructive suggestions for improving this manuscript. This work was supported in part by a grant from the Swiss National Science Foundation (3152A0-100431).

References

Arnold M. (1986): A propos des inclusions fluids monophasees dites metastables a temperature ambiante. *C. R. Acad. Sci., Paris*, **303**, 459-461.

Bakker, R.J. (2004): Raman spectra of fluid and crystal mixtures in the systems H2O, H2O-NaCl and H2O-MgCl2 at low temperatures: applications to fluid inclusion research. *The Canadian Mineralogist*, **42**, 1283-1314.

Bodnar R.J. & Sterner S.M. (1987): Synthetic fluid inclusions, *in* "Hydrothermal Experimental Techniques", G.C. Ulmer and H.L. Barnes, eds., J. Wiley & Sons, New York, 423-457.

Boiron M.C., Cathelineau M., Banks D.A., Buschaert S., Fourcade S., Coulibaly Y., Michelot, J.L., & Boyce A. (2002): Fluid transfers at a basement/cover interface Part II. Large-scale introduction of chlorine into the basement by Mesozoic basinal brines. *Chemical Geology*, **192**, 121-140.

Boyd, R.W. (2003): Nonlinear Optics. 2nd ed. Academic Press, San Diego, 578 p.

Debenedetti, P.G. (2003): Supercooled and glassy water. *Journal of Physics: Condensed Matter*, **15**, R1669-R1726.

Debenedetti, P.G. (2004): Reply to Comment on 'Supercooled and glassy water'. *Journal of Physics: Condensed Matter*, **16** (2004), 6815-6817.

Goldstein R.H. & Reynolds T.J. (1994): Are fluid inclusions representative samples of diagenetic

fluids? *and* Fluid inclusion microthermometry, *in* "Systematics of fluid inclusions in diagenetic minerals. SEPM short course. 31." Society for Sedimentary Geology. Tulsa, Oklahoma, 43-63 *and* 87-121.

Joglekar A.P., Liu H-h., Meyhöfer E., Mourou G. & A.J. Hunt (2004): Optics at critical intensity: Applications to nanomorphing. *Proceedings of the National Academy of Sciences of the USA*, **101**, 5856-5861.

Jonsson, E. & Broman, C. (2002): Fluid inclusions in late-stage Pb-Mn-As-Sb mineral assemblages in the Långban deposit, Berglagen, Sweden. *The Canadian Mineralogist*, **40**, 47-65.

Koechner, W. (1999): Solid-state laser engineering. 5th ed. Springer, Berlin, 746 p.

Newell K.D. & Goldstein R.H. (1999): A new technique for surface and shallow subsurface paleobarometry using fluid inclusions: an example from the Upper Ordovician Viola Formation, Kansas, USA. *Chemical Geology*, **154**, 97-111.

Novotny L. & Hecht B. (2006): Principles of Nano-Optics. Cambridge University Press, Cambridge, 539 p.

Poole P.H., Sciortino, U., Essman, H., & Stanley, H. (1992): Phase behaviour of metastable water. *Nature*, **360**, 324-328.

Potter R.W., II, Clynne M.A. & Brown D.L. (1978): Freezing point depression of aqueous sodium chloride solutions. *Economic Geology*, **73**, 284-285.

Roedder, E. (1984): Interpretation and utilization of inclusion measurements: metastability. *in* "Fluid inclusions. Reviews in Mineralogy, Vol. 12", Mineralogical Society of America, Chelsea, Michigan, 291-304.

Roedder, E. & Belkin, H.E. (1988): Significance of monophase fluid inclusions in minerals. *C. R. Acad. Sci., Paris*, **306**, 283-287.

Samson I.M. & Walker R.T. (2000): Cryogenic Raman spectroscopic studies in the system NaCl-$CaCl_2$-H_2O and implications for low-temperature phase behavior in aqueous fluid inclusions. *The Canadian Mineralogist*, **38**, 35-43.

Sastry, S., Debenedetti, P.G., Sciortino, F., & Stanley, H.E. (1996); Singularity-free interpretation of the thermodynamics of supercooled water. *Physical Review E*, **53**, 6144-6154.

Schaffer C.B., Nishimura N. & Mazur E. (1998): Thresholds for femtosecond laser induced breakdown in bulk transparent solids and water. *Proceedings of the SPIE*, **3451**, 2-8.

Speedy R.J. (1982): Stability-Limit Conjecture. An interpretation of the properties of water. *Journal of Physical Chemistry*, **86**, 982-991.

Speedy R.J. (2004): Comment on 'Supercooled and glassy water'. *Journal of Physics: Condensed Matter*, **16**, 6811-6813.

Sterner S.M., Hall D.L. & Bodnar R.J. (1988): Synthetic fluid inclusions. V. Solubility relations in

the system NaCl-KCl-H_2O under vapour-saturated conditions. *Geochim. Cosmochim.Acta.*, **52**, 989-1005.

Stoller P., Krüger Y., Rička J. & Frenz M. (2007): Femtosecond lasers in fluid inclusion analysis: three-dimensional imaging and determination of inclusion volume in quartz using second harmonic generation microscopy. *Earth and Planetary Science Letters*, **253**, 359-368.

Stuart B.C., Feit M.D., Herman S., Rubenchik A.M., Shore B.W., & Perry M.D. (1996): Nanosecond-to-femtosecond laser induced breakdown in dielectrics. *Physical Review B*, **53**, 1749-1761.

Török P., Varga P., Laczik Z. & Broker G.R. (1995): Electromagnetic diffraction of light focused through a planar interface between materials of mismatched refractive indices: an integral representation. *Journal of the Optical Society of America A*, **12**, 325-332.

Vogel A., Noack J., Hüttman G., & Paltauf G. (2005): Mechanisms of femtosecond laser nanosurgery of cells and tissues. *Appl. Phys. B*, **81**, 1015-1047.

Weisbrod A., Leroy, J. (1987): Comportement metastable des inclusions fluids monophasées dans les minéraux des roches. Conséquences. *C. R. Acad. Sci*., *Paris*, **305**, 455-459.

Zheng Q., Durben D.J., Wolf G.H. & Angell C.A. (1991): Liquids at large negative pressures: water at the homogeneous nucleation limit. *Science*, **254**, 829-832.

Figure captions

Figure 1 Sketch of the experimental setup showing the path of the laser beam used for phase nucleation and the transmitted white light used for imaging. The dichroic mirror reflects most of the 800 nm laser light, but a small fraction of the laser light back-scattered by the sample is transmitted and is visible on the camera, allowing determination of the location of the laser spot on the sample.

Figure 2.1 Laser induced bubble nucleation in a metastable aqueous one-phase inclusion in quartz at room temperature. (a) The one-phase inclusion before the laser pulse and (b) and (c) after the laser pulse. The position of the laser spot is indicated. (b) shows initial nucleation of two vapour bubbles, which recombine within the time required for a camera exposure (1/30 s) in the next frame in the acquired image series (c). This represents the thermodynamically stable phase state at room temperature. (L = liquid phase, V = vapour phase).

Figure 2.2 Laser induced bubble nucleation in a metastable aqueous one-phase inclusion in calcite at room temperature. (a) and (b) show the one-phase inclusion and the position of the bright laser spot before, and (c) and (d), after the laser pulse and nucleation of the vapour bubble. (c) and (d) show the thermodynamically stable phase state at room temperature. (L = liquid phase, V = vapour phase).

Figure 3.1 Laser induced nucleation of the vapour bubble (V) in a fluid inclusion in quartz with metastable phase assemblage (liquid (L) and ice) at – 14.0 °C (4.1 °C below $T_m ice$). (a) shows the liquid phase and the rounded ice crystal and the position of the bright laser spot before, and (b)-(d), after the laser pulse and nucleation of the vapour bubble (this represents the thermodynamically stable phase state at this temperature).

Figure 3.2 Laser induced nucleation of the vapour bubble (V) in a low saline fluid inclusion in quartz with metastable phase assemblage (liquid (L) and ice) at – 1.4 °C (0.5 °C below $T_m ice$). (a) shows the liquid phase and the ice crystals before, (b)-(d), after the laser pulse and nucleation of the vapour bubble (this represents the thermodynamically stable phase state at this temperature).

Figure 4.1 Laser induced nucleation of sylvite from a supersaturated KCl solution at room temperature (host mineral: quartz). (a) shows the metastable phase assemblage with liquid (L) and the vapour bubble (V) before the laser pulse. The position of the laser spot is indicated. (b) shows a tiny sylvite nucleus induced by the laser pulse and (c)-(e) illustrate continuous precipitation of sylvite from the solution and recrystallization until a thermodynamically stable phase state is achieved.

Figure 4.2 Laser induced nucleation of halite from a supersaturated NaCl solution at room temperature (host mineral: quartz). (a) The metastable phase assemblage with liquid (L) and the vapour bubble (V) before the laser pulse. The position of the laser spot is indicated. (b) The formation of two small secondary vapour bubbles resulting from the emission of a pressure wave caused by sub-microscopic quartz ablation at the surface of the inclusion by the femtosecond laser pulse. (c) and (d) show the subsequent nucleation and precipitation of halite.

Figure 4.3 Laser induced nucleation of ice and hyrohalite ($NaCl{\cdot}2H_2O$) in a supercooled, supersaturated NaCl solution at – 56.0 °C (host mineral: quartz). (a) shows the metastable phase assemblage with liquid (L) and the vapour bubble (V) before, and (b)-(f), after the laser pulse. (b) and (c) show the crystallization of ice whereas in (d)-(f) the crystallization of hydrohalite can be observed as a propagation of the phase boundary due to crystal growth. The vapour bubble is

strongly compressed due to volume expansion of the ice and the hydrohalite. On subsequent heating, ice and hydrohalite re-crystallize (g) and at the eutectic temperature of the binary H_2O-NaCl system (21.2 °C) ice melts completely and hydrohalite remains in the stable phase (h)-(j). On further heating, (k) and (l), hydrohalite in a thermodynamically stable state should dissociate at the peritectic temperature of + 0.1 °C under simultaneous formation of halite. Since the nucleation of halite failed hydrohalite remained metastable up to 20.2 °C.

Figure 5 Diagram showing the normalized threshold pulse energies necessary to achieve ablation of quartz as a function of depth within the sample as measured for different microscope objectives (see text for details).

Figure 6.1 Laser induced bubble nucleation in a supersaturated H_2O-NaCl one-phase inclusion at room temperature. The pulse energy corresponds to approximately 50 % of the energy used for visible quartz ablation in the bulk material at the same depth within the sample. (a) was obtained before and (b) after the laser pulse. (L = liquid phase, V = vapour phase).

Figure 6.2 Simultaneous nucleation of the vapour bubble and halite in a supersaturated H_2O-NaCl one-phase inclusion at room temperature induced by a single laser pulse. The pulse energy corresponds to approximately 70 % of the energy used for visible quartz ablation in the bulk material at the same depth within the sample. (a) before and (b) and (c), after the laser pulse. (L = liquid phase, V = vapour phase).

Figure 7.1 Nucleation of the vapour bubble in a supersaturated H_2O-NaCl one-phase inclusion at room temperature induced by a single laser pulse focused in the quartz close to the inclusion. The pulse energy used is approximately 6 % above the ablation threshold at the same depth within the

sample. (a) Metastable one-phase inclusion before the laser pulse. The position of the laser spot and of some ablation spots from previous experiments are indicated. (b) Nucleation of three vapour bubbles in the inclusion and the newly formed ablation spot caused by the laser pulse. The vapour bubbles recombine rather slowly; two bubbles in (c) form a single bubble (not shown). (L = liquid phase, V = vapour phase).

Figure 7.2 Nucleation of halite in the same supersaturated H_2O-NaCl inclusion containing liquid and vapour at room temperature induced by a single laser pulse focused in the quartz close to the inclusion. The pulse energy used is approximately 30 % above the ablation threshold at the same depth within the sample. Image (a) shows the metastable two-phase inclusion before the laser pulse. The position of the laser spot and some ablation spots from previous experiments are indicated. (b) and (c) show the nucleation and subsequent crystallization of halite after the laser pulse as well as the newly formed ablation spot generated by the laser pulse. (L = liquid phase, V = vapour phase).

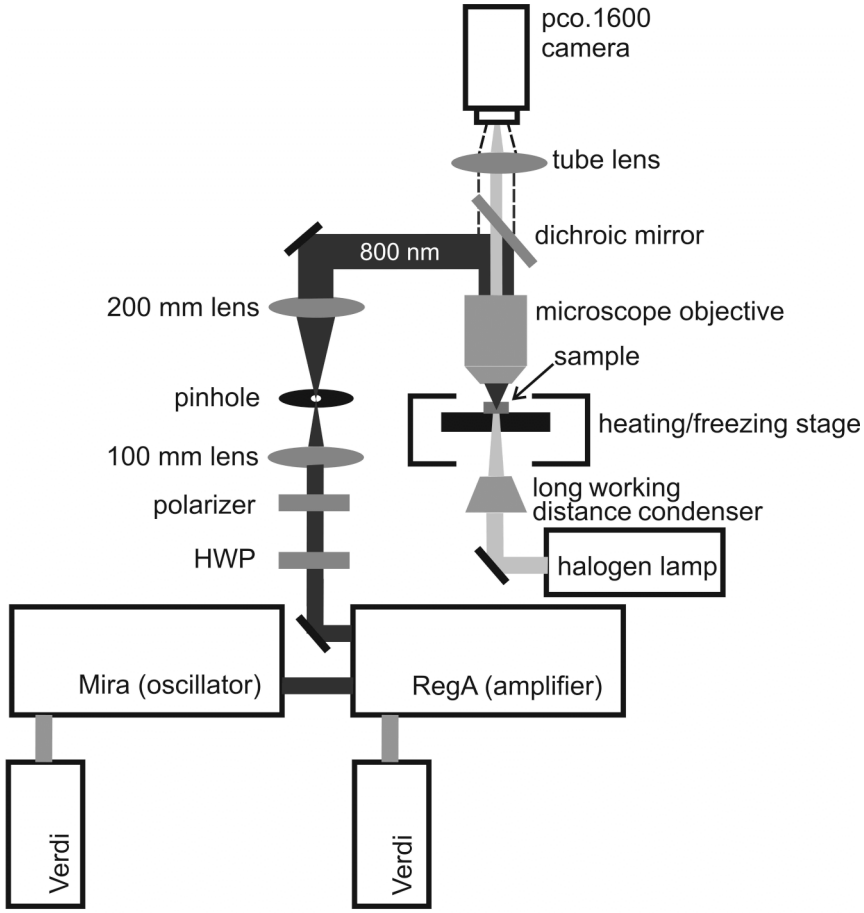
pco.1600
camera
tube lens
dichroic mirror
800 nm
200 mm lens
microscope objective
sample
pinhole
heating/freezing stage
100 mm lens
polarizer
long working
distance condenser
HWP
halogen lamp
Mira (oscillator)
RegA (amplifier)
Verdi
Verdi

Figure 1

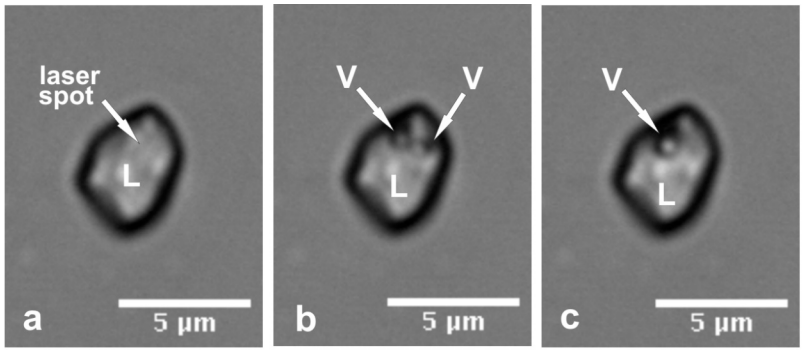

Figure 2.1

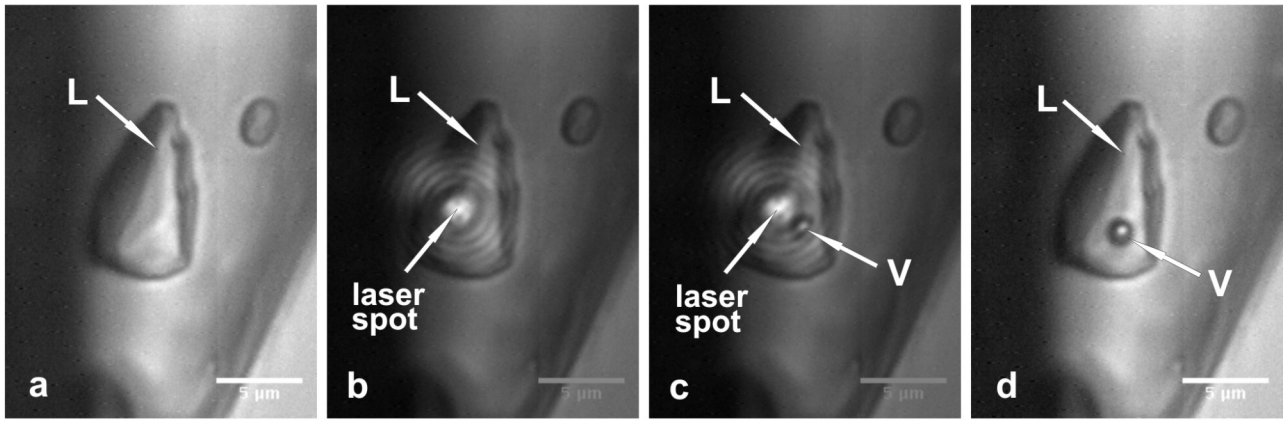

Figure 2.2

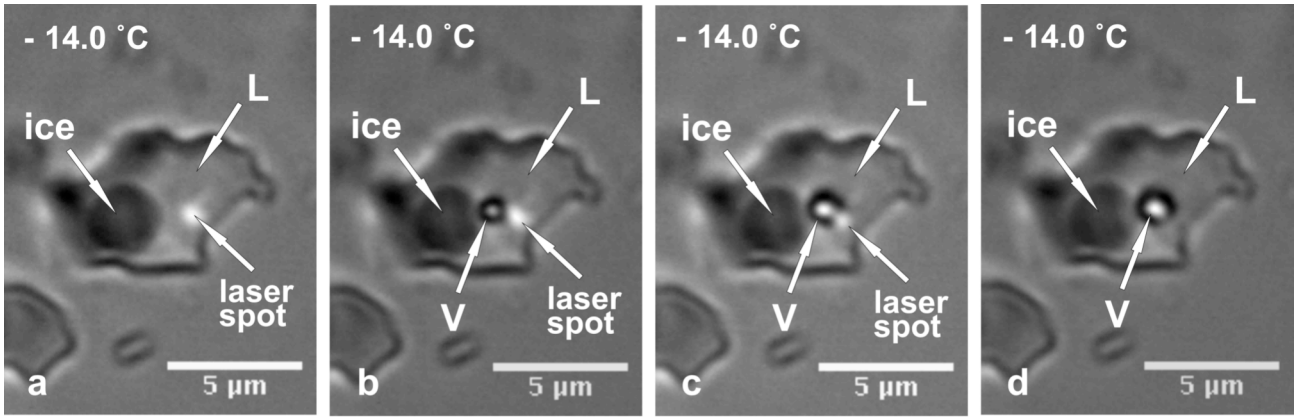

Figure 3.1

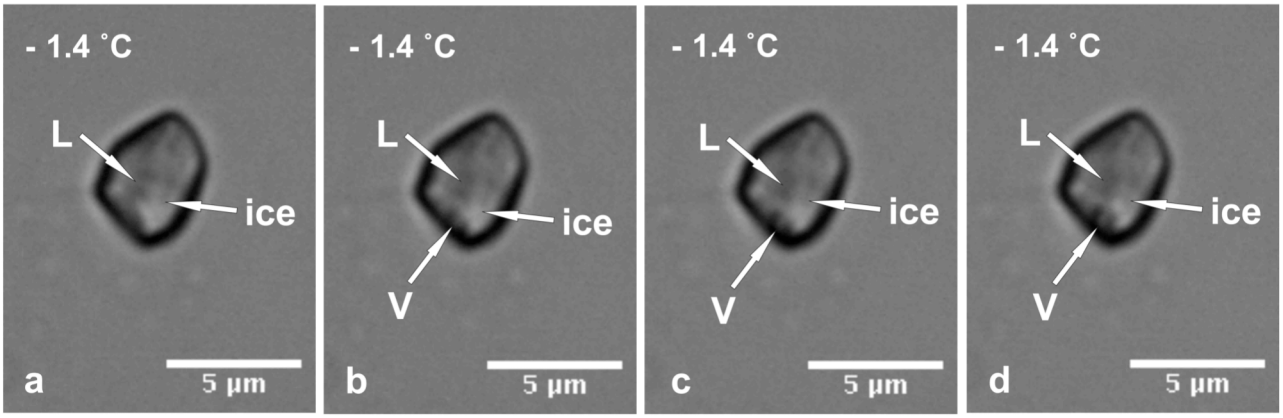

Figure 3.2

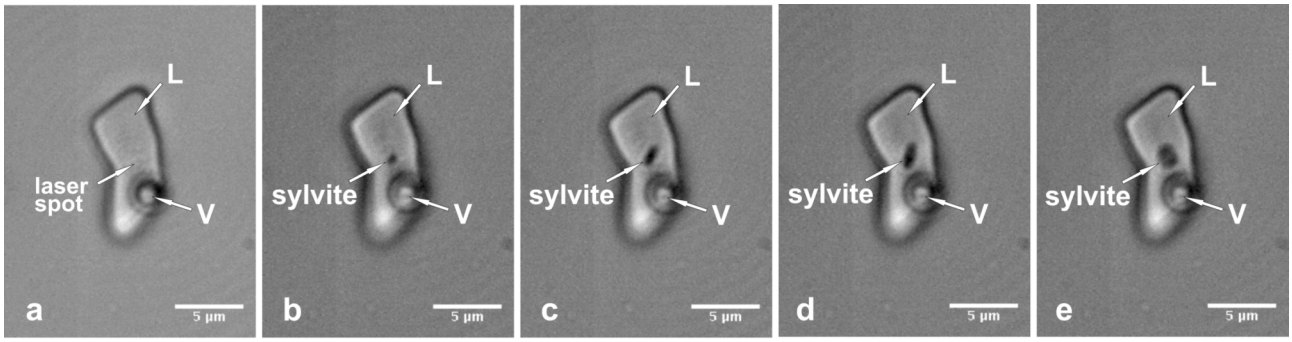

Figure 4.1

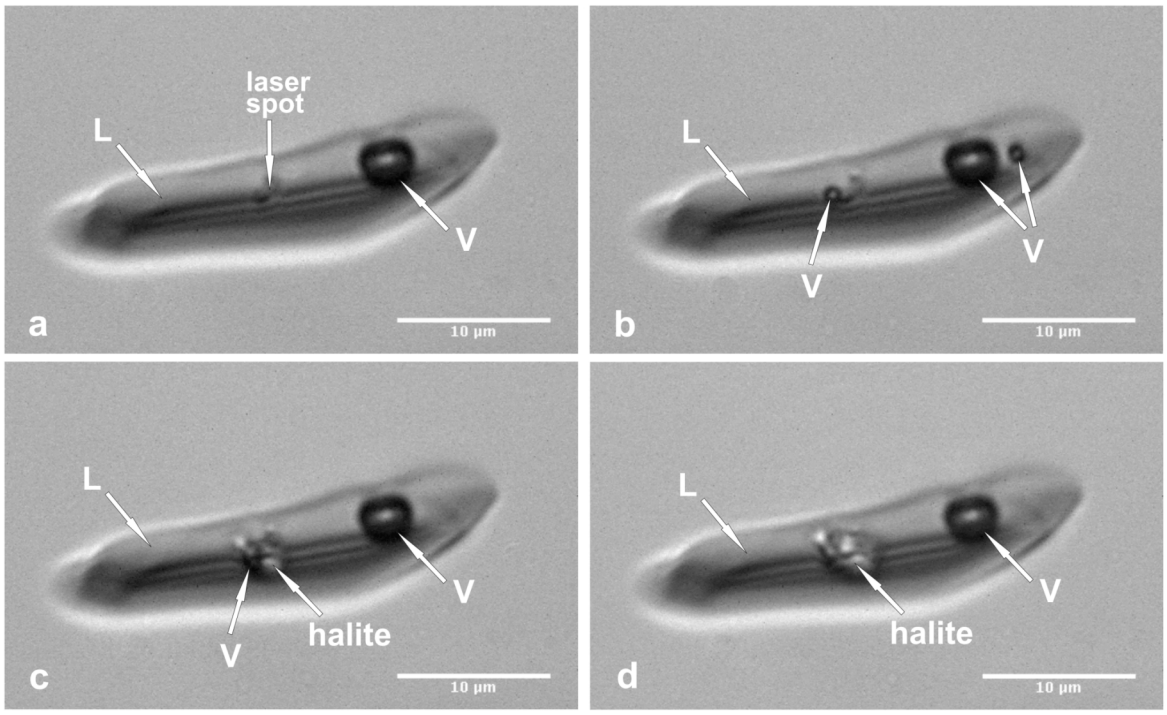

Figure 4.2

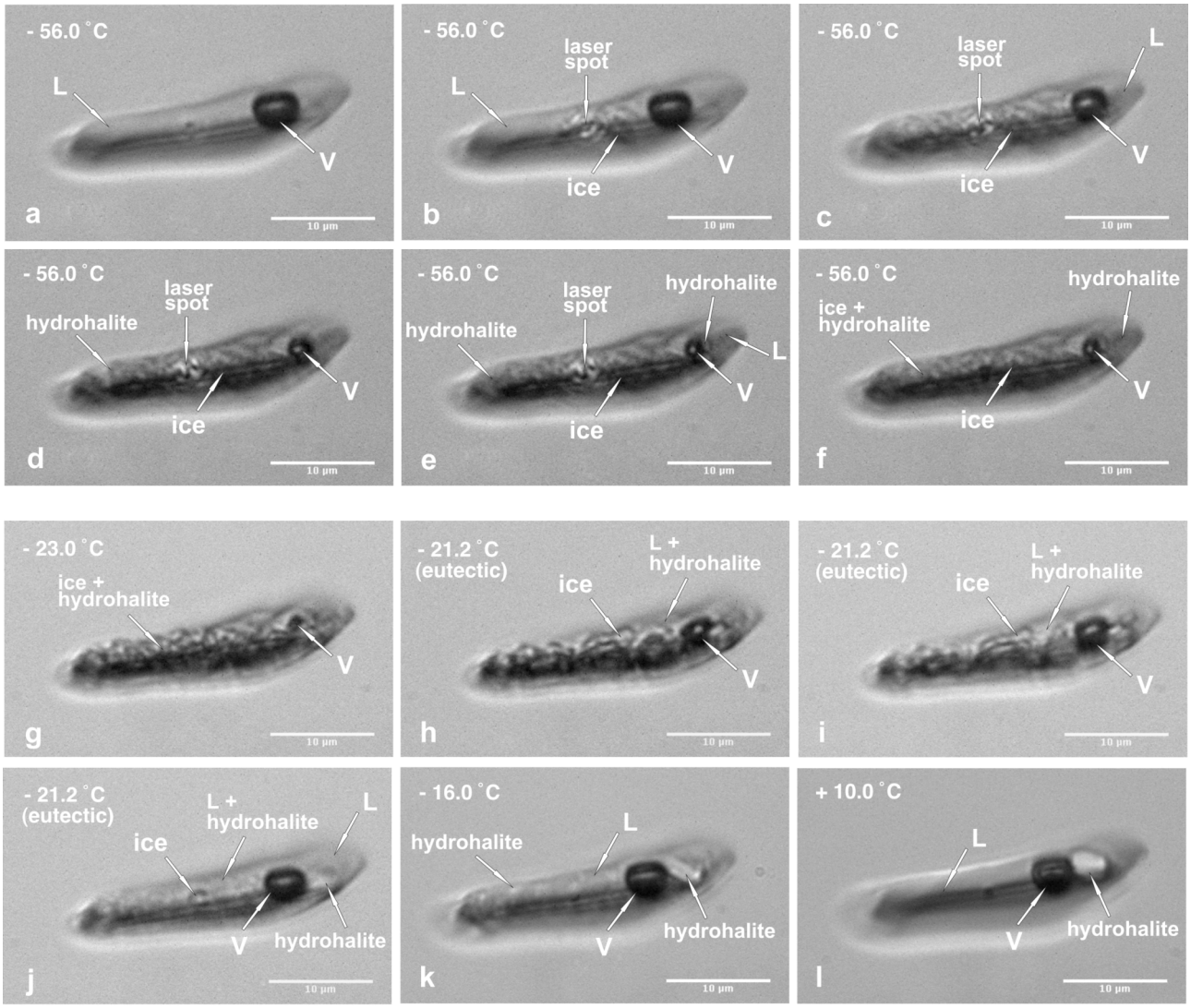
- 56.0 °C
L
V
a
10 µm
- 56.0 °C
laser spot
L
V
ice
b
10 µm
- 56.0 °C
laser spot
L
V
ice
c
10 µm
- 56.0 °C
hydrohalite
laser spot
V
ice
d
10 µm
- 56.0 °C
hydrohalite
laser spot
hydrohalite
L
V
ice
e
10 µm
- 56.0 °C
ice + hydrohalite
hydrohalite
V
ice
f
10 µm
- 23.0 °C
ice + hydrohalite
V
g
10 µm
- 21.2 °C (eutectic)
ice
L + hydrohalite
V
h
10 µm
- 21.2 °C (eutectic)
ice
L + hydrohalite
V
i
10 µm
- 21.2 °C (eutectic)
ice
L + hydrohalite
L
V
hydrohalite
j
10 µm
- 16.0 °C
hydrohalite
L
V
hydrohalite
k
10 µm
+ 10.0 °C
L
V
hydrohalite
l
10 µm

Figure 4.3

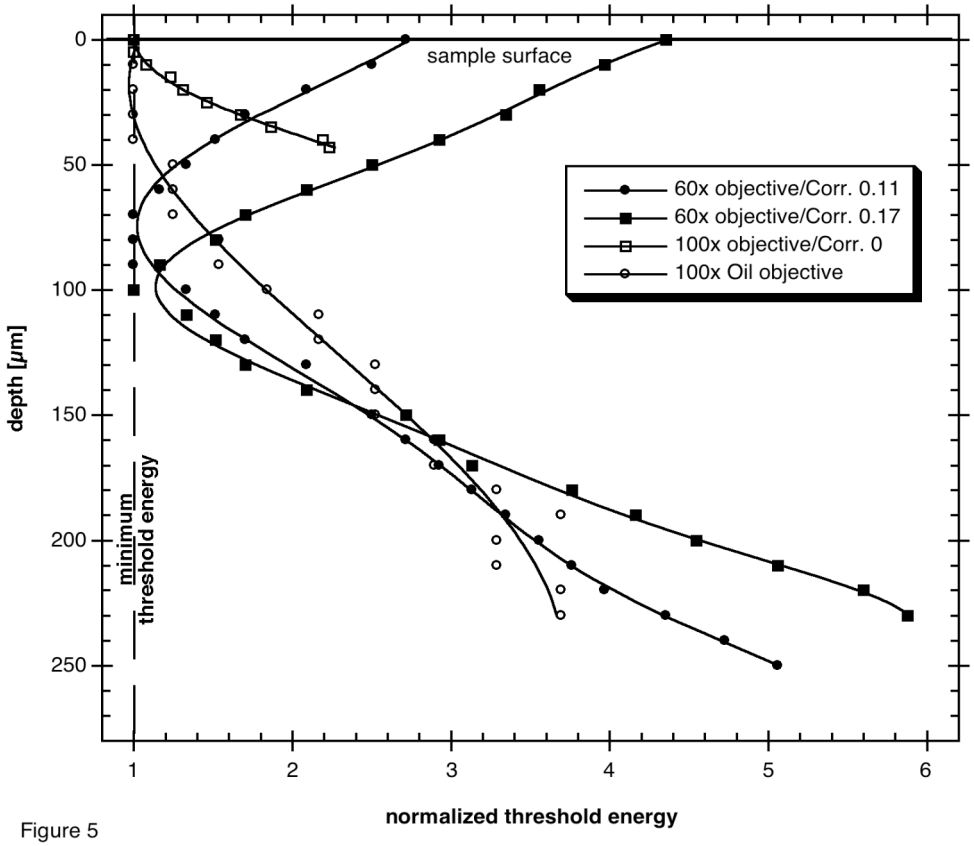
0
50
100
150
200
250
depth [µm]
sample surface
60x objective/Corr. 0.11
60x objective/Corr. 0.17
100x objective/Corr. 0
100x Oil objective
minimum
threshold energy
1
2
3
4
5
6
normalized threshold energy

Figure 5

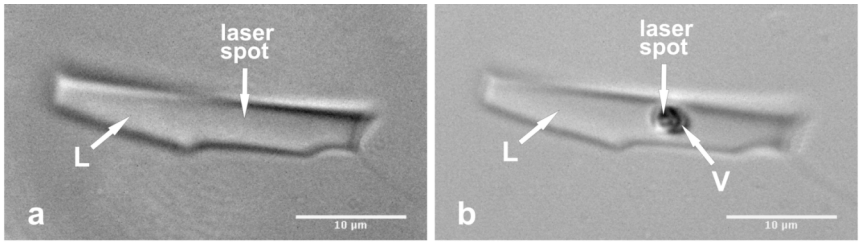

Figure 6.1

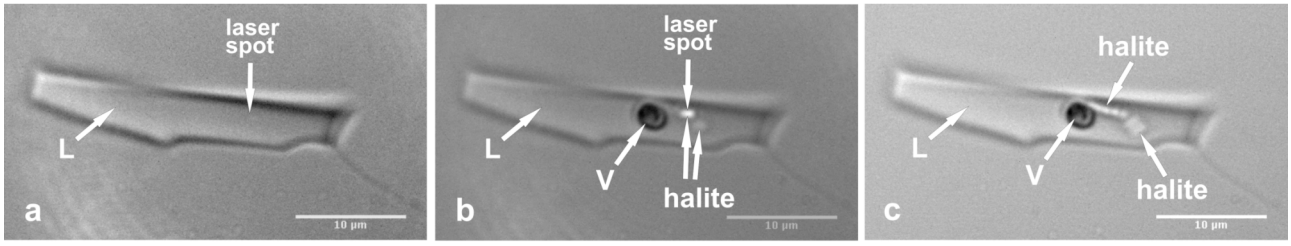

Figure 6.2

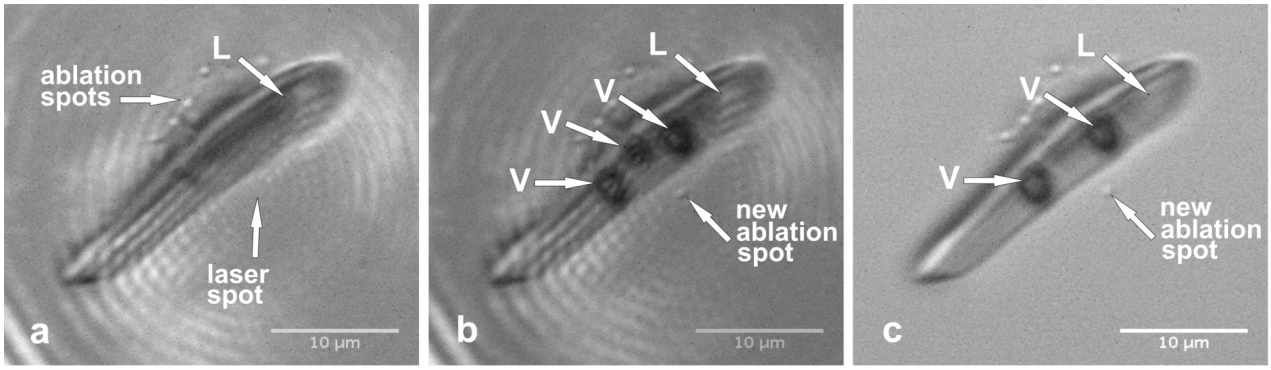

Figure 7.1

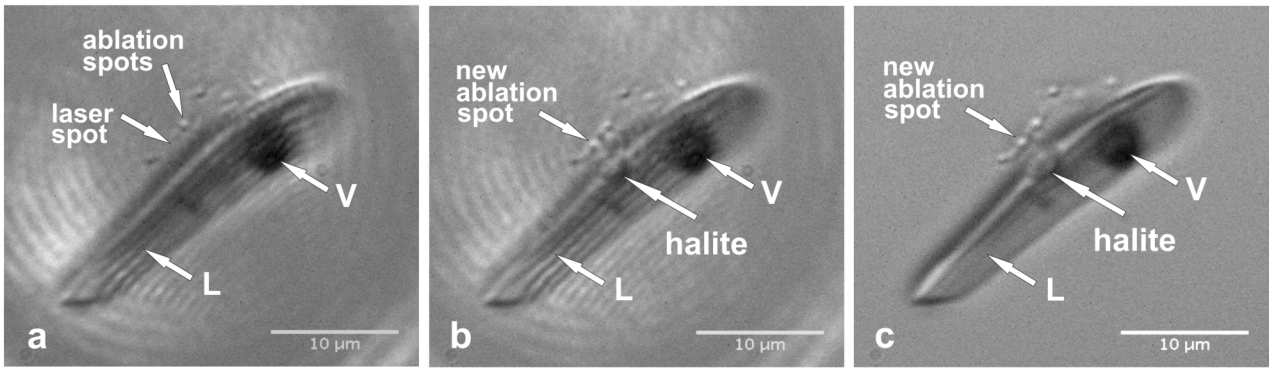

Figure 7.2